


Cite this: *RSC Adv.*, 2025, 15, 33615

# Photochemical synthesis of Pd nanocatalysts stabilized by biomass-derived polymers: from colloidal to supported systems in batch and flow

Irina Della-Cagnoletta,<sup>ID</sup><sup>ab</sup> Silvia M. Soria-Castro,<sup>ID</sup><sup>\*ab</sup> Fabrizio Politano,<sup>ID</sup><sup>ab</sup>  
Sandra E. Martín,<sup>ID</sup><sup>ab</sup> Paula M. Uberman,<sup>ID</sup><sup>\*ab</sup> and Gabriela Oksdath-Mansilla,<sup>ID</sup><sup>\*ab</sup>

This study reports a novel light-driven methodology for the sustainable synthesis of Pd-based nanocatalysts. The approach features operational simplicity, short reaction times, and environmental friendliness. The visible light-induced reduction of Pd<sup>2+</sup> precursors, allowed for the efficient production of both colloidal and silica-supported palladium nanoparticles (Pd-NPs), stabilized with either polyvinylpyrrolidone (PVP) or carboxymethylcellulose (CMC). The method was successfully implemented in batch and continuous-flow systems, demonstrating excellent scalability and control over the nanoparticle size (<5 nm) of Pd-NPs. The synthesized nanocatalysts exhibited excellent catalytic performance in Suzuki–Miyaura cross-coupling reactions under mild conditions, achieving turnover frequencies (TOFs) of 3733 h<sup>−1</sup> for Pd-CMC NPs and 3126 h<sup>−1</sup> for Pd-PVP NPs. For heterogeneous catalysts, *in situ* photoreduction was identified as the most effective immobilization strategy, producing highly active and uniformly dispersed Pd-NPs on silica nanoparticles (SNPs). These supported catalysts showed high recyclability, minimal Pd leaching, and consistent catalytic performance over multiple cycles. XPS and FT-IR characterization confirmed the presence of CMC and citrate as key stabilizing agents in the nanocatalysts, providing insight into the surface chemistry and stability of the materials. Furthermore, the successful implementation of a continuous-flow methodology for both colloidal and supported systems highlights the method's scalability and control over nanoparticle morphology. Overall, this work highlights the robustness and versatility of the photochemical strategy, offering a green and practical route to reusable Pd nanocatalysts for modern catalytic applications.

Received 13th July 2025  
Accepted 6th September 2025

DOI: 10.1039/d5ra05019g

rsc.li/rsc-advances

## 1 Introduction

Palladium is a key catalyst in a wide range of chemical processes, including C–C and C–heteroatom bond formation, as well as hydrogenation and oxidation reactions.<sup>1</sup> Its remarkable versatility arises from its ability to adopt multiple oxidation states, enabling the formation of organometallic complexes, nanoparticles (NPs), and extended surfaces. In particular, Pd nanoparticles (Pd-NPs) are recognized as exceptional catalysts due to their high surface-to-volume ratio, which maximizes the availability of reactive surface atoms and significantly enhances catalytic efficiency. Moreover, Pd-NPs can improve the thermal, mechanical, and barrier properties of materials.<sup>2,3</sup> Both colloidal and supported Pd-NPs have emerged as promising

materials for the development of heterogeneous catalysts. Consequently, the development of controlled and efficient synthetic strategies is crucial for fully exploiting the unique properties of metal-based nanoparticles.

The widespread use of metal NPs in industries such as electronics, agriculture, and healthcare, has driven the development of various synthetic methodologies that enable precise control over NPs morphology. This allows for the tailoring of NPs into diverse shapes (such as spheres, rods, and quantum dots), thereby expanding their potential applications and fostering technological innovation.<sup>4</sup> In this context, the development of reliable synthetic methods that offer precise control over the morphology, composition, and surface properties of metal NPs is crucial for their successful implementation.

Moreover, the synthesis of NPs presents significant opportunities for the application of green chemistry principles. To achieve more sustainable NP production, it is essential to employ nontoxic, hydrophilic stabilizing agents and environmentally friendly reducing agents.<sup>5–7</sup> In this context, several sustainable approaches have been developed for the synthesis of Pd-NPs, including: (i) the use of environmentally friendly solvents, like glycerol-derived solvents used to produce Pd-NPs;<sup>8</sup>

<sup>a</sup>Universidad Nacional de Córdoba, Facultad de Ciencias Químicas, Departamento de Química Orgánica, Haya de la Torre y Medina Allende. Edificio Ciencias 2. Ciudad Universitaria X5000HUA, Córdoba, Argentina. E-mail: ssoriacastro@unc.edu.ar; paula.uberman@unc.edu.ar; gabriela.oksdath@unc.edu.ar

<sup>b</sup>Instituto de Investigaciones en Físicoquímica de Córdoba-INFIQC-CONICET-Universidad Nacional de Córdoba, Haya de la Torre y Medina Allende. Edificio Ciencias 2. Ciudad Universitaria X5000HUA, Córdoba, Argentina



(ii) the use of less-hazardous reducing agents that minimize toxic byproducts, for example caffeine and plant-derived polyphenols have been used as both reducing and capping agents for Pd-NP synthesis;<sup>9</sup> and (iii) the selection of appropriate capping or dispersing agents that ensure NPs stability while being non-toxic and biodegradable. Ideal capping agents should exhibit high water solubility, low toxicity, biocompatibility, thermal stability, and the ability to control crystal growth and module NP morphology.<sup>10</sup>

For instance, polyvinylpyrrolidone (PVP) polymer is one of the most widely used stabilizers for Pd-NPs and fulfills these criteria; however, it is derived from the oil-industry. Biodegradable polymers, particularly polysaccharides such as cellulose,<sup>11</sup> pectin,<sup>12,13</sup> chitosan<sup>14</sup> and collagen,<sup>15</sup> among others,<sup>16</sup> have shown excellent performance in stabilizing metal-NPs and can also act as reducing agent. For example, Pd-NPs stabilized by sodium hyaluronate have been used as colloidal catalyst for the rapid reduction of azo dyes for water decontamination.<sup>17</sup> A heterogeneous catalyst based on Pd-NPs deposited on a cellulose-Fe<sub>3</sub>O<sub>4</sub>-graphene oxide composite was evaluated in Heck and Sonogashira coupling reactions, showing good activity and recyclability.<sup>18</sup> Additionally, Pd-NPs stabilized with 2-hydroxyethylcellulose and immobilized on ZnO<sub>2</sub> demonstrated high selectivity in the hydrogenation of alkynes.<sup>19</sup>

Among various stabilizing agents, sodium carboxymethyl cellulose (CMC-Na), a widely used water-soluble cellulose derivative, is particularly attractive due to its ability to interact with several metal ions through the numerous hydroxyl and carboxymethyl groups present along its polymer chains. This characteristic makes CMC an ideal support for metal NPs. Several reports have demonstrated the ability of CMC to support and stabilize Pd nanocatalyst.<sup>20–23</sup> Recently, CMC-based nanomaterials have been employed as catalysts in C–C cross-coupling and hydrogenation reactions, exhibiting high catalytic activity.<sup>24–27</sup> These results underscore the potential of CMC as a versatile and efficient stabilizing agent, warranting further investigation.

Nevertheless, certain challenges remain in the development of sustainable methodologies for the preparation of highly active nanocatalysts. For instance, many existing approaches require elevated temperatures for the reduction of metal salts, the use of strong reducing agents, or prolonged reaction times to obtain well-dispersed Pd-NPs. Additionally, these methods often yields materials with low Pd loading or weak metal-support interactions, which can compromise catalyst recovery and reusability, thereby increasing operational costs and limiting the overall sustainability of the process.<sup>22</sup>

Green synthesis approaches using plant extracts or microorganisms offer a promising route for the eco-friendly production of metal nanocatalysts.<sup>28,29</sup> However, several experimental challenges, such as the selection of appropriate biological materials, the precise control of synthesis conditions, and the assurance of product quality, hinder the transition to large-scale industrial applications. One promising approach involves the development of visible-light induced NPs synthesis, which provides a more controlled and sustainable method for fabricating nanoscale material.<sup>30</sup> For example, the photoinduced

synthesis of Ag-NPs using plant extracts under visible light has proven to be a cost-effective and environmentally friendly alternative to traditional methods.<sup>31</sup>

Consequently, catalyst preparation methods that enable precise control over particle size, morphology, and metal composition are essential for enhancing catalytic performance. In this context, continuous-flow technology, particularly when combined with photochemical approaches, has emerged as a robust, reproducible, and versatile method for the fabrication NPs<sup>30</sup> and nanocatalysts.<sup>32,33</sup> Moreover, the reduced volumes of solvent and reagents, along with precise control of temperature, pressure, and mass transfer in flow reactors, make these systems safer and more efficient than large-scale batch reactors.<sup>34</sup>

Although Pd-NPs have been synthesized using continuous-flow systems, few studies have explored their formation under visible-light irradiation.<sup>35</sup> We recently reported the rapid synthesis of small colloidal Pd nanocatalysts *via* photoreduction of a Pd<sup>2+</sup>–citrate/oxalate complexes under blue-LED light, achieving monodisperse Pd-NPs in just two minutes under flow conditions with excellent catalytic performance.<sup>36</sup> This method avoids the use of toxic and hazardous chemical reducing agents and solvents, and allows for the efficient reduction of the Pd<sup>2+</sup>, providing a green route for the synthesis of Pd nanocatalysts.

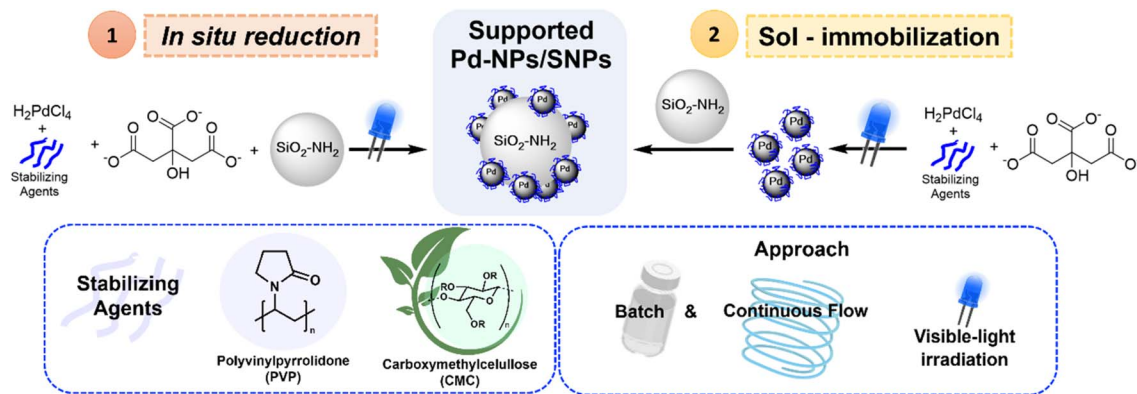
With the aim of designing a new type of heterogeneous catalyst in a more sustainable and efficient manner, we extended our photochemical approach by employing bio-based reducing and stabilizing agents under mild conditions. Pd-NPs stabilized with either CMC or PVP were prepared in water *via* photoreduction of a Pd<sup>2+</sup> salts by citrate/oxalate, and immobilized onto APTES-functionalized SiO<sub>2</sub> nanoparticles (SNPs). Notably, we report for the first time the synthesis of Pd/SNPs *via* continuous photo-flow process (Scheme 1). All nanocatalysts were characterized and evaluated in the Suzuki–Miyaura cross-coupling reaction, exhibiting excellent catalytic efficiency and good reusability for several reaction cycles. These results demonstrate that the developed photochemical methodology allows for the straightforward preparation of highly active heterogeneous nanocatalysts under green conditions.

## 2 Experimental methods

### 2.1. General materials

All chemicals were reagent grade and were used as received from the manufacturer. Palladium(II) chloride (PdCl<sub>2</sub>, Anedra), hydrochloric acid (HCl 37% w/w), ammonium hydroxide (NH<sub>4</sub>OH, 28% w/w), trisodium citrate dihydrate (Sigma-Aldrich®); disodium oxalate (Sigma-Aldrich®), poly(*N*-vinylpyrrolidone) polymer (Mw PVP = 10 000 Da), sodium carboxymethylcellulose (Sigma-Aldrich®, medium viscosity), tetraethyl orthosilicate (TEOS), (3-aminopropyl)-triethoxysilane (APTES), 4-bromoacetophenone, 4-iodoacetophenone, 4-chloroacetophenone, 4-iodoanisole, 4-bromoanisole, 2-iodoanisole, 4-iodobenzonitrile, 4-bromobenzonitrile, 3-bromoquinoline, phenylboronic acid, 4-fluorophenylboronic acid, K<sub>3</sub>PO<sub>4</sub>, ethanol 98% (Porta®) and anhydrous Na<sub>2</sub>SO<sub>4</sub> were used as received. All solvents were analytical grade and distilled





**Scheme 1** Proposed visible-light-induced methodologies for the synthesis of heterogeneous Pd-nanocatalysts under batch and continuous flow conditions.

before use.  $\text{H}_2\text{PdCl}_4$  feedstock 2 mM solution was prepared from analytical grade chemicals and Milli-Q-Millipore water. Suzuki–Miyaura cross coupling reactions were carried out under air atmosphere. Silica gel (0.063–0.200 mm) was used in column chromatography.

Photochemical reactions in batch were carried out in scintillation vials equipped with a magnetic bar and sealed with Teflon plugs. The mixtures were irradiated with a blue 5 W LED (462 nm) and stirred under argon atmosphere.

Photochemical reactions in flow were carried out in a meso-scale photochemical flow reactor (6.56 mL with 0.75 mm ID FEP-tubing) equipped with a blue-LED reactor (15 × 5 W at 462 nm). A battery-powered magnetic stirrer (Cole-Parmer™) was used for the flow experiments.

## 2.2. Characterization of Pd nanocatalysts

TEM images were obtained using TEM Hitachi HT7800 120 kV microscope operating at 80 kV, available at the Centro de Microscopía Electrónica Facultad de Ciencias Médicas, UNC in Córdoba, Argentina. Samples for morphological characterization were prepared by depositing a drop of the colloidal suspension on a 300 mesh formvar-carbon coated copper grid and dried at room temperature. SEM microscopy was performed in a SEM – Zeiss Sigma 360 (Lamarx-UNC). Size distribution of Pd-NPs was established by the average over 100 NPs from different places at each image of all samples. Distribution plots of the size were resolved by fitting data with a Gaussian behavior.

FT-IR spectra were recorded on a Nicolet iN10 IR Microscope (Thermo Scientific). For FT-IR analysis samples contained in KBr discs were scanned from 400 and 4000  $\text{cm}^{-1}$ , and the recording conditions were: normal resolution, sample scan, 64  $\text{s}^{-1}$ . The spectra were analyzed using OMNIC 8 software-ThermoFischer.

ICP-MS analysis was performed on an Agilent 7500cx Spectrometer equipped with an Agilent ASX-500 Series autosampler, using argon as carrier gas, available at ICYTAC-CONICET-UNC in Córdoba, Argentina. Pd and Re (185) signals were simultaneously recorded as internal standards for each sample. All

aqueous samples were digested before injection using  $\text{HNO}_3$  for 18 h at room temperature.

XPS spectra were performed in a Thermo Scientific K-Alpha X-ray photoelectron spectrometer system (LAMARX, FaMAF-UNC), equipped with a hemispherical energy analyzer and a monochromated X-ray source was used for surveying the photoemission spectra. The base pressure measured in the main chamber was in the low  $10^{-9}$  mbar range. The photoionization of the samples was induced by monochromatized Al K $\alpha$  photons at 1486 eV. The XPS spectrum was adjusted to the main spurious C 1s peak at 284.8 eV. To avoid any charging effects during measurement (typically observed in semiconductor-isolated systems), a flood gun to compensate the charge was used. The overcompensation effects by adjusting the spectra during measurement were also tested.

## 2.3. Synthesis of colloidal Pd-PVP and Pd-CMC NPs

In a 10 mL scintillation vial equipped with a magnetic stir bar, 25–100 mg of PVP (0.5–2.0 w/v (%)) or 12.5–50.0 mg of CMC (0.25–1.0 w/v (%)); 29.4 mg of sodium citrate (molar ratio  $\text{Pd}^{2+}/\text{reducing agent}$  1 : 10) and 5 mL of a 2 mM feedstock aqueous solution of  $\text{H}_2\text{PdCl}_4$  were placed. When CMC was used as a stabilizing agent, the solution was stirred for 30 min until the polymer was fully hydrated. The vial was sealed and high purity Ar bubbled for 5 min to saturate the solution. Next, the vial was placed into the photochemical reactor and was irradiated under vigorous magnetic stirring until the mixture color changes to dark brown solution. Finally, the vial was opened to the air, and the Pd-PVP or Pd-CMC NPs dispersions were stored in a falcon tube to be used as catalyst solution without further purification.

## 2.4. Representative procedure for the Suzuki–Miyaura cross-coupling reaction catalyzed by colloidal Pd-NPs

Into a 10 mL tube reaction with a Teflon screw-cap septum equipped with a magnetic stirrer 4-bromoacetophenone (0.25 mmol), phenylboronic acid (0.35 mmol) and  $\text{K}_3\text{PO}_4$  (0.75 mmol) were placed. Then, EtOH (0.5 mL) and water (to obtain a total volume of 1.5 mL taking into account the volume of Pd-NPs solution) were added. At last, the 52  $\mu\text{L}$  of Pd-NPs 2 mM

(0.04 mol%) was added. The reaction mixture was heated in an oil bath for 1 h. After being cooled to room temperature, the mixture was opened to the air, diluted with water and then extracted three times with ethyl acetate (5 mL each). The biaryl product was purified by silica-gel column chromatography after being dried with anhydrous  $\text{Na}_2\text{SO}_4$ . The product was quantified by GC employing benzophenone as internal standard. The pure product was compared with authentic samples by GC, GC-MS and  $^1\text{H}$  NMR. All the spectroscopic data were in agreement with those previously reported for the product 1-(biphenyl-4-yl) ethanone.<sup>37</sup>

## 2.5. Methodology approaches for the preparation of supported Pd-NPs onto SNPs and characterization

The synthesis of the supported nanocatalysts was performed following two approaches: (a) sol-immobilization of Pd-PVP or Pd-CMC NPs onto SNPs and (b) synthesis *in situ* of Pd-NPs in presence of SNPs and stabilizer. Both approaches were performed under batch and continuous flow systems.

**2.5.1. Sol-immobilization of Pd-PVP or Pd-CMC NPs onto SNPs in batch.** In a 250 mL round bottom flask equipped with a magnetic stir bar, 90 mL of water was added and adjusted to pH 1 with  $\text{H}_2\text{SO}_4$  2 M feedstock solution. Then, 10 mL of colloidal solution of Pd-NPs was added, stirred for 5 min and then 200 mg of SNPs were added. The mixture was stirred overnight to obtain Pd-CMC-im-1/SNPs or 30 min to obtain Pd-CMC-im-2/SNPs and Pd-PVP-im/SNPs. The supported catalyst was recovered through centrifugation for 8 min at 3500 rpm. The supernatant was stored for ICP-MS analysis, and the solid was washed with water. This procedure was repeated two times. Finally, the supported catalyst with a grey color was dried under air at room temperature for 24 h. After this procedure, 120 mg of nanocatalyst was recovered to further be used in catalysis.

**2.5.2. Synthesis *in situ* of Pd-NPs in presence of SNPs under batch conditions.** In a 10 mL scintillation vial equipped with a magnetic stir bar, 5 mL of a mixture of stabilizer (PVP or CMC), reducing agent (citrate and/or oxalate salts) and  $\text{H}_2\text{PdCl}_4$  2 mM was prepared following the same protocol for the synthesis of colloidal Pd NPs. Then, 10.1 mg of SNPs were added, the vial was sealed and Ar bubbled for 5 min to saturate the solution. Next, the mixture was irradiated in the photochemical reactor under vigorous magnetic stirring until it changed color to brown. Finally, the vial was opened, and the supported catalyst was recovered through centrifugation.

**2.5.3. Sol-immobilization of Pd-PVP or Pd-CMC NPs onto SNPs in continuous flow system.** A colloidal solution of Pd-PVP (2.0 w/v (%)) or Pd-CMC (0.5 w/v (%)) NPs (48 mL, 2 mM) was charged into a plastic syringe. On the other hand, 30 mg of SNPs were suspended in 48 mL water, adjusted to pH = 1 with  $\text{H}_2\text{SO}_4$  2 M and loaded into a second plastic syringe with a stir bar inside. The syringe pump together with a portable magnetic stirrer bar were placed in vertical position in order to keep the SNPs suspension as much homogenous as possible and to avoid clogging. Both syringes were connected through a mesoscale photochemical flow reactor (6.56 mL with 0.75 mm ID PFA-tubing) and the mixture was continuously pumped into the

reactor by using the syringe pump ( $0.109 \text{ mL min}^{-1}$ ) at room temperature. Finally, the heterogeneous material was collected and the supported catalyst was recovered through centrifugation for 8 min at 3500 rpm. The supernatant was stored for ICP-MS analysis, and the solid was washed with water. This procedure was repeated two times. Finally, the supported catalyst with a grey color was dried under air at room temperature for 24 h.

**2.5.4. Synthesis *in situ* of Pd-PVP NPs in presence of SNPs in continuous flow system.** A mixture of solution of PVP (2.0 w/v (%)), sodium citrate and sodium oxalate salts (molar ratio  $\text{Pd}^{2+}/$  reducing agent 1 : 10) and 48 mL of feedstock aqueous solution of  $\text{H}_2\text{PdCl}_4$  4 mM, was saturated by Ar and charged into a syringe. On the other hand, 30 mg of SNPs were suspended in 48 mL water, adjusted to pH = 1 with  $\text{H}_2\text{SO}_4$  2 M saturated by Ar and charged into a second plastic syringe with a stir bar inside. The syringe pump together with a portable magnetic stirrer bar were placed in vertical position in order to keep the SNPs suspension as much homogenous as possible and to avoid clogging. Both syringes were connected through a mesoscale photochemical flow reactor (6.56 mL with 0.75 mm ID PFA-tubing) and the mixture was continuously pumped and irradiated for 30 min through a blue-LED reactor ( $15 \times 5 \text{ W}$  at 462 nm). Finally, the heterogeneous material was collected in an open glass vial to ensure that the reaction stops. The supported catalyst was recovered through centrifugation for 8 min at 3500 rpm. The supernatant was stored for ICP-MS analysis, and the solid was washed with water. This procedure was repeated two times. Finally, the supported catalyst with a grey color was dried under air at room temperature for 24 h.

**2.5.5. Representative procedure for the Suzuki-Miyaura cross-coupling reaction catalyzed by supported Pd nanocatalysts.** Into a 10 mL tube reaction with a Teflon screw-cap septum equipped with a magnetic stirrer, 4-bromoacetophenone (0.12 mmol), arylboronic acid (0.18 mmol) and  $\text{K}_3\text{PO}_4$  (0.37 mmol), and 1.0 mg of the supported Pd-NPs catalyst was added. Then, EtOH (0.7 mL) and water (2.0 mL) were added. The reaction mixture was heated at  $60^\circ\text{C}$  in an oil bath for 2 h. After being cooled to room temperature, the mixture was opened to the air, diluted with water. Then, 0.05 mmol of benzophenone was added to the mixture of organic phase and aqueous supernatant, and it was extracted using  $2 \times 5 \text{ mL}$  of ethyl acetate. The organic phase was dried with anhydrous  $\text{Na}_2\text{SO}_4$  and analysed by gas chromatography. To recover the heterogeneous nanocatalyst, the aqueous phase was centrifuged at 3500 rpm for 8 min. The moles of Pd in each reaction to calculate the TOF values were obtained from the Pd loading of each catalyst determined by ICP-MS analysis.

## 3 Results and discussion

### 3.1. Visible-light induced synthesis of colloidal Pd-NPs with PVP and CMC as stabilizing agents

Recently, we developed a simple and straightforward photochemical method to synthesize Pd-NPs stabilized by PVP polymer, which exhibited outstanding catalytic activity in the Suzuki-Miyaura cross-coupling reaction under mild reaction





conditions.<sup>36</sup> The Pd-PVP nanocatalysts were synthesized in batch by irradiating an aqueous solution of  $\text{H}_2\text{PdCl}_4$  with sodium citrate for 1 h using a blue-LED light. This procedure yielded small Pd-NPs with a mean diameter of  $(2.8 \pm 0.8)$  nm. The resulting colloidal dispersion was stable and could be stored in air for several months without significant changes.

With the aim of improving the sustainability of the process, we evaluated the effect of modifying the stabilizing agent on the photochemical synthesis of Pd-NPs. CMC-Na was selected as an alternative biomass-derived stabilizing agent. A comparative analysis between PVP and CMC was conducted to assess the influence of the stabilizing agent on Pd-NPs formation (Table 1). Both, the type and concentration of the polymer, were examined to obtain small-sized NPs with narrow size distribution and good colloidal stability. TEM analysis was employed to determine the size of the NPs in each sample (Fig. 1, SI 2 and SI 3).

Starting with PVP as stabilizer, we evaluated Pd-NPs formation at polymer concentrations of 2.0, 1.0, and 0.5 w/v (%) (Table 1, entries 1–3). A reduction in the amount of the stabilizing agent led to the formation of progressively larger NPs. As the polymer concentration decreases, its ability to effectively cap the growing NPs diminishes, allowing the particles to grow larger and, in some cases, to form aggregates. For example, at a PVP concentration of 0.5 w/v (%), Pd-PVP NPs with an average size of  $(4.7 \pm 0.9)$  nm were obtained (Fig. 1a), and aggregation of individual NPs was observed in TEM micrographs (Fig. 1a and SI 2).

Subsequently, CMC was evaluated as a stabilizing agent. The main drawback of CMC is the increased viscosity of the resulting solutions due to their gelation properties.<sup>21</sup> Therefore, lower concentrations of CMC (up to 1 w/v (%)) were examined for the Pd-NPs synthesis. Using this biomass-derived polymer, the characteristic brown colloidal dispersion of Pd-NPs was

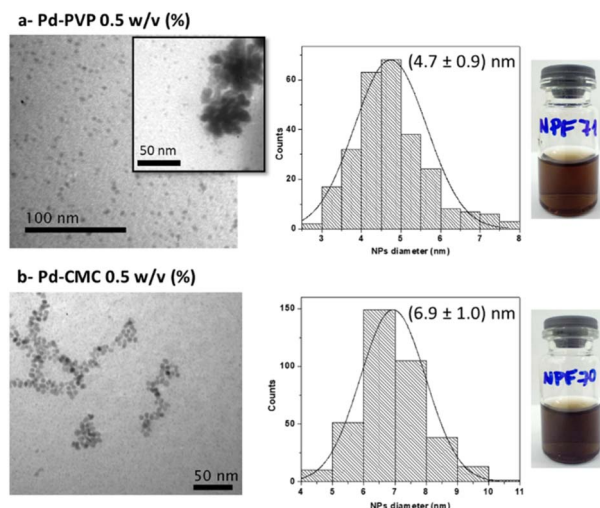


Fig. 1 TEM images and size distribution of Pd-NPs stabilized with 0.5 w/v (%) of (a) PVP and (b) CMC.

observed after 1.5 h of irradiation. As shown TEM micrographs in Fig. 1b and SI 3, the use of CMC as a stabilizer resulted in the formation of spherical Pd-CMC NPs with slightly larger diameters compared to those obtained with PVP (Table 1, entries 4–6). Moreover, in this case, the size of Pd-NPs increased with the amount of CMC, suggesting that a higher polymer concentration led to a reduced rate of nuclei formation and enhanced NPs growth. This effect may be attributed to the tendency of CMC to form self-aggregates at higher concentrations,<sup>30</sup> rather than interacting with the metal surface. This behavior reduces its effectiveness as a stabilizing agent and leads to the formation of larger NPs, as previously reported in the literature.<sup>38</sup> The optimal CMC concentration for obtaining Pd-NPs with low polydispersity was found to be 0.5 w/v (%). Under these conditions, Pd-CMC NPs with a mean diameter of  $(6.9 \pm 1.0)$  nm were obtained after 1.5 h of irradiation (Fig. 1b).

In addition, control experiments were conducted (Table 1, entries 7–8). When the reaction was carried out for 1.5 h under dark conditions, the original yellowish  $\text{H}_2\text{PdCl}_4$  solution was recovered (Fig. SI 4c). Under this condition, no reduction of  $\text{Pd}^{2+}$  occurs, and the absence of Pd-NPs was confirmed by TEM analysis. These results confirm that the formation of Pd-NPs is initiated by light irradiation.

A mixture of  $\text{H}_2\text{PdCl}_4$  and CMC was irradiated for 3.5 h to evaluate the effect of the absence of citrate as the photo-reductant agent (Table 1, entry 7). After this time, the characteristic brown colloidal dispersion of Pd-NPs was observed (Fig. SI 4d). TEM analysis revealed the formation of large aggregates ( $\sim 50$  nm) along with a few Pd-NPs with mean diameter of  $(5.3 \pm 1.6)$  nm (Fig. SI 3c). Considering that the CMC structure contains carboxylate and hydroxyl functional groups, it is plausible that these groups interact with  $\text{Pd}^{2+}$  ions and initiate the photoreduction process.<sup>22</sup> To support this, we analyzed the UV-vis spectra of the different samples (Fig. SI 4a and b). A blue shift in the absorption band of the  $\text{H}_2\text{PdCl}_4$  was observed: from 418 nm to 397 nm in the presence of CMC, and

Table 1 Photochemical synthesis of Pd-NPs in presence of PVP and CMC as stabilizing agents<sup>a</sup>

Entry	Stabilizer			
	Name	w/v (%)	Time (h)	NPs diameter <sup>b</sup> (nm)
1	PVP	2.0	1	$(2.8 \pm 1.0)$
2		1.0	1	$(3.2 \pm 0.7)$
3		0.50	1	$(4.7 \pm 0.9)$
4	CMC	1.0	1.5	$(7.0 \pm 1.5)$
5		0.50	1.5	$(6.9 \pm 1.0)$
6		0.25	1.5	$(5.1 \pm 1.1)$
7 <sup>c</sup>		0.50	3.5	Large aggregates
8 <sup>d</sup>		0.50	1.5	—

<sup>a</sup> Reaction conditions: 5 mL of  $\text{H}_2\text{PdCl}_4$  2 mM, 10 eq. of sodium citrate, the proper amount of stabilizer, 40 °C, Ar, 5 W blue LED. <sup>b</sup> Determined by TEM analysis. <sup>c</sup> Without sodium citrate. <sup>d</sup> Under dark conditions.



from 418 nm to 386 nm in the presence of both CMC and citrate (Fig. SI 4a). These shifts suggest the formation of different  $\text{Pd}^{2+}$  complexes, indicating an interaction between  $\text{Pd}^{2+}$  and the carboxylate or hydroxyl groups of CMC, which may be contribute to the photoreduction mechanism similarly to that of citrate.<sup>36</sup> After 3.5 h of irradiation the UV-vis spectrum shows an increase in the absorption band, characteristic of Pd-NPs (Fig. SI 4b). Although CMC can reduce  $\text{Pd}^{2+}$  and stabilize the resulting NPs, in the absence of citrate, large aggregates of Pd-NPs were obtained (Fig. SI 3c).

Then, Pd-CMC NPs (with 0.5% of CMC) were further characterized using DLS, FT-IR, and  $^1\text{H}$  NMR, techniques. The apparent hydrodynamic diameter ( $d_{\text{H}}$ ) of Pd-CMC NPs was measured by DLS (Fig. SI 7), revealing a monodisperse distribution of Pd-NPs with an average size of  $(12.2 \pm 1.9)$  nm. The  $d_{\text{H}}$  value reflects not only the core size of the NPs, but also the hydration layer and the adsorbed polymer on their surface.

The interaction between CMC and Pd-NPs was investigated by FT-IR analysis of the mixtures before and after irradiation, as well as their precursors (Fig. SI 5). The characteristic bands corresponding to both the polymer and citrate were observed in the spectrum of the Pd-CMC NPs. A broad band around  $\sim 3400\text{ cm}^{-1}$  in all samples was assigned to the stretching vibrations of hydroxyl groups ( $-\text{OH}$ ) from citrate and CMC, while the bands observed at 2920, and  $2856\text{ cm}^{-1}$  were attributed to the stretching vibration of aliphatic C-H bonds. In the Pd-CMC NPs spectrum, bands at 1596 and  $1409\text{ cm}^{-1}$  correspond to the asymmetric and symmetric stretching vibrations of carboxylate groups ( $-\text{COO}^-$ ) from CMC, while the bands between 1104 and  $1065\text{ cm}^{-1}$  are associate with C-O-C stretching modes, consistent with literature data.<sup>39</sup> A comparison of the spectra obtained before and after irradiation showed no change in the carboxylate absorption bands; however, a slight shift was observed in the  $-\text{OH}$  stretching band. These spectral features are essential for evaluating the interactions between the polymer and the NPs. In particular, the separation between asymmetric and symmetric carboxylate bands ( $\Delta$ ) provides insight into the coordination mode between the metal and the carboxylate groups.<sup>40,41</sup> In both samples, before and after irradiation,  $\Delta$  values were 188 and  $187\text{ cm}^{-1}$ , respectively, indicating a bidentate coordination of both  $\text{Pd}^{2+}$  and  $\text{Pd}^0$  species to the  $\text{COO}^-$  groups.<sup>40,41</sup> Additionally, in the Pd-CMC NPs sample, the hydroxyl stretching vibration band of CMC shifted from  $3440$  to  $3424\text{ cm}^{-1}$ , suggesting a hydrogen bonding interactions between the  $-\text{OH}$  groups and the Pd-NP surface, according to literature.<sup>40,41</sup> These observations confirm the interaction between CMC and Pd-NPs.

Since the interaction between the Pd species and citrate could not be ruled out, we analyzed the  $^1\text{H}$  NMR spectra of the samples before and after irradiation (Fig. SI 6). The signals observed around 2.7–2.5 ppm correspond to the methylene protons of citrate. The spectra revealed a slight downfield shift of these signals in the presence of Pd species, suggesting a coordination interaction between Pd and citrate. In addition, the signals corresponding to the CMC backbone appear around 4.8–3.0 ppm,<sup>39</sup> with no appreciable change in their chemical

shift after irradiation, indicating that the CMC structure remained largely unaltered during the process.

Thus, the observed changes in UV-vis absorption bands, FT-IR spectra, and  $^1\text{H}$  NMR signals indicate coordination interactions between  $\text{Pd}^{2+}$  and both citrate and CMC, suggesting that these ligands are involved in the reduction of  $\text{Pd}^{2+}$ . Furthermore, we confirmed the presence of CMC and remaining citrate in the final NPs, indicating that the photoreductant agent is not completely consumed during the reaction and may also contribute to the stabilization of Pd-NPs.

The photochemical strategy proved to be a simple and efficient method for generating small Pd-NPs in the presence of CMC, offering a sustainable alternative to PVP. Although the use of CMC resulted in slightly larger NPs compared to those obtained with PVP, the Pd-CMC NPs exhibited good colloidal stability, demonstrating that CMC is a suitable capping agent for Pd-NPs. However, for catalytic applications, it is crucial to ensure that the stabilizer modification does not negatively affect the catalyst's performance. Therefore, the catalytic activity of the colloidal Pd-NPs was evaluated in Suzuki–Miyaura cross-coupling reaction between 4-bromoacetophenone (**1a**) and phenylboronic acid (**2a**) (Fig. 2 and see SI Table SI 1). Based on our previous study,<sup>36</sup> the reactions were carried out under mild conditions, using  $\text{K}_3\text{PO}_4$  as base in an ethanol–water solvent mixture at  $40^\circ\text{C}$  for 1 h.

As shown in Fig. 2, all colloidal Pd-NPs exhibited excellent catalytic activity under mild reaction conditions, achieving high yields ( $>90\%$  of **3a**) and elevated TOF values ( $>1900\text{ h}^{-1}$ ), regardless of the type or concentration of stabilizer used. Notably, these values are comparable to or even higher than those of other Pd-NPs reported in literature (Table SI 2).<sup>14,20,22,37,39,41–45</sup>

When comparing Pd-NPs stabilized with the same polymer, slight differences in catalytic activity were observed. For example, Pd-NPs synthesized with 1.0 w/v (%) PVP exhibited the highest catalytic activity. Although lower PVP concentration produced larger NPs, the decreased polymer coverage likely resulted in greater exposure of active sites, thereby enhancing catalytic activity. These findings suggest that NPs size alone

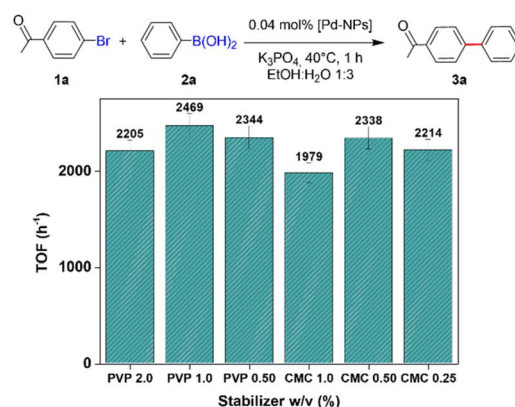


Fig. 2 Suzuki–Miyaura cross-coupling reaction catalyzed by Pd-NPs stabilized with CMC and PVP.



does not fully account for the observed catalytic behavior. Other factors such as surface chemistry and the nature of the stabilizing agents also play critical roles in determining catalytic performance. These parameters affect the accessibility of active sites, as well as the electronic properties and overall catalytic efficiency of the nanocatalysts. In this case, the optimal balance between NPs stabilization and catalytic activity was achieved with 1 w/v (%) PVP. A similar trend was observed for Pd-CMC NPs, with maximum catalytic activity obtained at a CMC concentration of 0.5 w/v (%).

To compare the performance of NPs stabilized with different polymers at the same concentration (PVP 0.5% vs. CMC 0.5%), catalytic tests were performed for both Pd-PVP and Pd-CMC nanocatalysts at 30 °C for 0.5 h (Table SI 3). Under this condition, Pd-CMC nanocatalyst yielded 68% of product **3a** with a TOF value of  $3733\text{ h}^{-1}$ , whereas the Pd-PVP NPs produced 61% of **3a** with a TOF of  $3126\text{ h}^{-1}$ . Thus, CMC as stabilizer not only provides a more sustainable alternative for nanomaterial synthesis but also enhances catalytic activity compared to PVP.

This photochemical approach thus demonstrated high efficacy in producing stable and highly active Pd nanocatalysts with tunable size, employing visible light as a green and energy-efficient method. However, the practical recovery of colloidal Pd nanocatalysts from the reaction mixture remains a significant challenge, as reported for similar Pd-NP systems.<sup>36,46</sup> Therefore, to advance in the development of nanocatalysts with high activity, easily recoverable and recyclable, we extended our photochemical strategy to the design of heterogeneous nanocatalysts, as discussed in the following section.

### 3.2. Immobilization of Pd-NPs onto silica supports (SNPs)

Solid-supported Pd nanocatalysts have demonstrated easy separation and excellent catalytic activity. Moreover, their catalytic properties can be optimized by improving stability, increasing surface area, enhancing reusability, and minimizing Pd use by maintaining or even enhancing catalytic activity.<sup>47–49</sup> Among inorganic supports, silica-derived materials ( $\text{SiO}_2$ ) exhibit a high specific surface area, excellent thermal and mechanical stability, and low cost. Therefore, silica is often used as a model support for metal loading and to investigate catalytic reaction mechanisms.<sup>50</sup> Silica nanoparticles functionalized with APTES (SNPs) are well-established amorphous materials for the immobilization of metal catalysts, as they promote the deposition of metallic NPs on their surface.<sup>51</sup> In addition, they are readily available and can be easily synthesized *via* the Stöber method.<sup>52,53</sup> Thus, SNPs were selected for the preparation of supported Pd nanocatalysts.

We explored two different approaches to generate heterogeneous Pd nanocatalysts (see Scheme 1): (i) sol-immobilization of the photochemically pre-synthesized Pd-NPs onto spherical SNPs,<sup>54,55</sup> and (ii) *in situ* photoreduction, in which Pd-NPs were formed and deposited directly onto the SNPs surfaces. Additionally, both approaches were performed in batch and continuous-flow set-up to evaluate their efficiency and reproducibility.

### 3.3. Sol-immobilization method for deposition of Pd-NPs onto SNPs under batch conditions

Based on the high catalytic activity of the Pd-CMC NPs 0.5 w/v (%) and our previous study to obtain colloidal Pd-PVP NPs 2.0 w/v (%),<sup>36</sup> these two NPs systems were selected for immobilization onto SNPs under batch conditions. Spherical SNPs with a mean diameter of  $(256 \pm 22)\text{ nm}$ , prepared *via* Stöber method, were used (see TEM analysis, Fig. SI 8).<sup>56</sup>

The immobilization conditions of the colloidal Pd-NPs onto SNPs were optimized by evaluating the Pd/SNPs mass ratio, temperature, and contact time for each stabilizing polymer (Table SI 4). For both stabilizers, the immobilization process successfully led to the formation of heterogeneous catalysts, with no change in Pd-NPs size observed after the impregnation process.

Immobilization using the Pd-PVP NPs solution resulted in the formation of the heterogeneous catalyst denoted Pd-PVP-im/SNPs (Table SI 4, entry 3). When performed at room temperature, the process resulted in a homogeneous distribution of Pd-NPs on the SNP surface (TEM micrograph, Fig. SI 10c).

Conversely, impregnation at room temperature using the Pd-CMC NPs solution produced the material Pd-CMC-im-1/SNPs (Table SI 4, entry 1), which exhibited aggregation of Pd-NPs on the SNPs surface (TEM micrograph, Fig. SI 9). This aggregation was attributed to the high viscosity of CMC polymer solutions at room temperature, which is influenced by electrostatic interactions and intermolecular hydrogen-bonds.<sup>57</sup> To improve Pd-NPs distribution on SNPs, both the synthesis and immobilization of Pd-CMC NPs were carried out at 50 °C, yielding the material Pd-CMC-im-2/SNPs (Table SI 4, entry 2). Under these conditions, smaller Pd-CMC NPs with a diameter of  $(4.5 \pm 1.0)\text{ nm}$  were obtained (TEM micrograph, Fig. SI 10a), along with a homogeneous distribution of NPs onto SNPs (TEM micrograph, Fig. SI 10b).

Regarding metal loading, a higher Pd content of 3.4 wt% was achieved using PVP as the stabilizer, compared to 0.8–1 wt% when using CMC, as determined by ICP-MS analysis (Table SI 4, entries 2–3).

### 3.4. *In situ* reduction method for the generation of Pd-NPs onto SNPs under batch conditions

As a second approach, the *in situ* photochemical reduction of  $\text{Pd}^{2+}$  salt onto SNPs was carried out using both stabilizer agents. Preliminary studies revealed that, in absence of a stabilizer, the *in situ* photoreduction of  $\text{Pd}^{2+}$  on SNPs led to the formation of large and non-uniform Pd-NPs (TEM micrograph, Fig. SI 11).

In contrast, the presence of either polymer enabled the successful deposition of uniformly distributed small Pd-NPs on the SNPs surface, as confirmed by TEM analysis (Fig. 3). To achieve efficient photoreduction, the  $\text{Pd}^{2+}$ /SNPs mass ratio had to be increased from 0.01 (used in the sol-immobilization process) to 0.10 to ensure an adequate light absorption at the working wavelength (462 nm) (Fig. SI 4a).

Regarding particle size, when the *in situ* synthesis was performed with CMC at 50 °C, the resulting Pd-CMC-is-1/SNPs



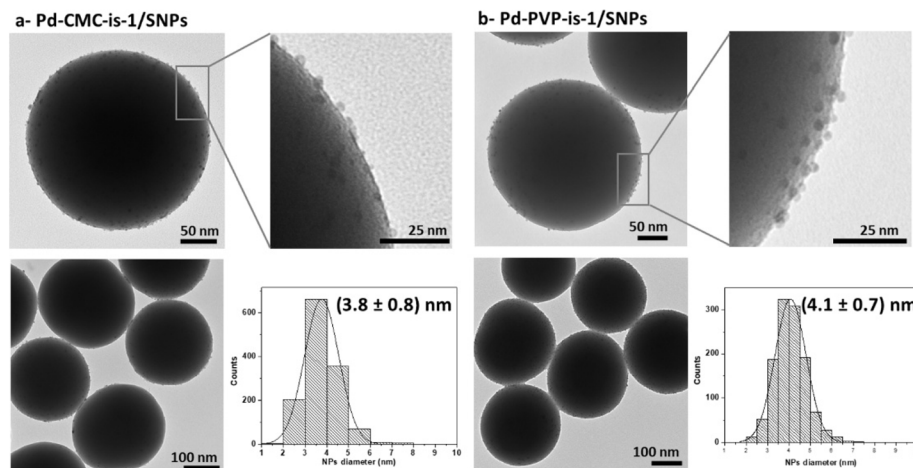


Fig. 3 TEM analysis of supported catalysts prepared through *in situ* photoreduction of  $\text{Pd}^{2+}$  salts on the SNPs in the presence of (a) CMC or (b) PVP. Zoom-in images show the Pd-NPs immobilized on the support.

nanomaterial (Table 2, entry 1) exhibited slightly smaller Pd-NPs (see TEM micrograph, Fig. 3a) compared to those obtained in the absence of SNPs (Fig. SI 10a). Conversely, when PVP was used as stabilizer (Pd-PVP-is-1/SNPs, Table 2, entry 3), larger Pd-NPs were obtained in the presence of SNPs (TEM micrograph, Fig. 3b).

In terms of Pd content, PVP again enabled a higher Pd loading on the support (Table 2, entries 1 vs. 3). To evaluate the maximum Pd loading achievable, the  $\text{Pd}^{2+}$ /SNPs mass ratio was increased up to 0.6, resulting in Pd loadings of 5.9 and 22.8 wt% for CMC and PVP, respectively (Table 2, entries 2 and 4).

The as-obtained supported nanocatalysts were also characterized by SEM, SEM-EDS, FT-IR and XPS (see Fig. SI 12–14). SEM images of both materials showed that the SNPs maintained their uniform and dense morphology (SEM micrographs, Fig. SI 13a and SI 14a). The EDS analysis confirmed the homogeneous distribution of Pd throughout the material, along with the presence of Si, O, and C (EDS spectra, Fig. SI13b and SI 14b).

The FT-IR spectra of each sample displayed the characteristic bands of the polymers and SNPs (Fig. SI 13c and SI 14c). The broad band at  $3400\text{ cm}^{-1}$  corresponds to the stretching of O–H groups of SNPs, while the strong absorption band at  $1108\text{ cm}^{-1}$  corresponds to the stretching of Si–O–Si bond. For the Pd-PVP-is-2/SNPs (Fig. SI 13c), the amide stretching band was shifted from  $1663\text{ cm}^{-1}$  in pure PVP to  $1627\text{ cm}^{-1}$  in the

nanocatalyst, suggesting coordination between the PVP polymer and Pd species. Similarly, in Pd-CMC-is-2/SNPs sample (Fig. SI 14c), the carboxylate stretching band shifted slightly from  $1617$  (pure CMC) to  $1629\text{ cm}^{-1}$ , indicating an interaction between Pd species and CMC polymer.

XPS analyses were conducted to determine the oxidation state of Pd in both nanomaterials (see Fig. SI 13d and SI 14d). For the PVP-stabilized catalyst, the Pd 3d spectrum exhibited two main peaks corresponding to the  $3d_{5/2}$  and  $3d_{3/2}$  transitions, each of which was further deconvoluted into two components (Fig. SI 13d). By comparison with previously report of Pd-PVP NPs, this corresponds to the presence of Pd in two oxidation states:  $\text{Pd}^0$  (334.1 and 339.3 eV) and a small fraction of  $\text{Pd}^{2+}$  (336.2 and 341.5 eV) in a ratio  $\text{Pd}^0/\text{Pd}^{2+}$  94 : 6. The presence of  $\text{Pd}^{2+}$  species has been attributed to interactions between the amide groups of PVP and Pd species, which can lead to more electron-deficient Pd species.<sup>58</sup> In contrast, the XPS spectrum of the CMC-stabilized nanocatalyst showed only two peaks, with binding energies (BE) at 335.9 and 341.3 eV (Fig. SI 14d), indicating the presence of a single Pd species ( $\text{Pd}^0$ ). Previous studies have reported a shift in the  $3d_{5/2}$  peak to higher binding energies in Pd-CMC NPs, with values around 335.4 eV for  $\text{Pd}^0$  and 337.1 eV for  $\text{Pd}^{2+}$  species.<sup>21</sup> This confirms the effective reduction of  $\text{Pd}^{2+}$  salts to  $\text{Pd}^0$  in Pd-CMC/SNPs catalysts. Moreover, the differences observed in the chemical environments of both catalysts provide additional evidence of interactions between

Table 2 Synthesis of Pd-CMC-is/SNPs and Pd-PVP-is/SNPs catalysts by *in situ* methodology under batch conditions<sup>a</sup>

Entry	Name	Stabilizer w/v (%)	<i>T</i> (°C)	NPs diameter <sup>c</sup> (nm)	Pd loading <sup>d</sup> (wt%)
1	Pd-CMC-is-1/SNPs	CMC 0.5%	50	(3.8 ± 0.8)	1.6
2 <sup>b</sup>	Pd-CMC-is-2/SNPs			(3.5 ± 0.8)	5.9
3	Pd-PVP-is-1/SNPs	PVP 2.0%	20	(4.1 ± 0.7)	2.9
4 <sup>b</sup>	Pd-PVP-is-2/SNPs			(4.7 ± 1.1)	22.8

<sup>a</sup> *In situ* reduction conditions: 5 mL of  $\text{H}_2\text{PdCl}_4$  2 mM, sodium oxalate/citrate 9 : 1 eq., proper amount of stabilizer, 10.1 mg of SNPs, Ar, 30 min of irradiation using 5 W blue LED. Mass ratio  $\text{Pd}^{2+}$ /SNPs = 0.1. <sup>b</sup> Mass ratio  $\text{Pd}^{2+}$ /SNPs = 0.6. <sup>c</sup> Determined by TEM analysis. <sup>d</sup> Determined by ICP-MS analysis.





the polymers and the Pd-NPs immobilized on the SNPs, which may significantly influence their catalytic behavior.

In comparison with well-established methods for preparing heterogeneous nanocatalysts, such as the sol-immobilization of preformed NPs or the wet-impregnation method (which involves the deposition and subsequent reduction of metal salts precursors onto the support), traditional approaches often require strong reducing agents (e.g.  $\text{NaBH}_4$ ), long reaction times, and elevated temperatures to produce well-dispersed and uniform Pd-NPs.<sup>21,22,59</sup> In contrast, the *in situ* strategy developed in this study offers a fast and efficient alternative for producing small, highly dispersed Pd-NPs supported on SNPs. The method is carried out under mild conditions, using biocompatible reducing agents and aqueous media, and is characterized by short reaction times.

### 3.5. Supported Pd-NPs/SNPs nanocatalysts synthesis under continuous flow conditions

Continuous flow strategies were developed with the aim of evaluating potential improvements in the morphology, uniformity, and reproducibility of synthesized Pd-NPs. Based on the results from the previous section, key parameters such as time, reducing agent ratio and  $\text{Pd}^{2+}$ /SNPs mass ratio were systematically studied.

To achieve this, an operationally simple and versatile tubular reactor was designed, utilizing blue-LEDs irradiation as the light source (Fig. 4a). The flow reactor consisted of a transparent perfluoroalkoxy (PFA) capillary tube (750  $\mu\text{m}$  ID, 6.56 mL) coiled around a cylindrical reactor coated with aluminum foil. The reflective foil helped to maximize light exposure by redirecting incident light back into the reactor. The irradiation setup

featured 12 blue LEDs (see Experimental section, Fig. SI 1a and 1b for details) mounted on 4 heat exchangers surrounding the PFA capillary coil. The setup included two pumps for the injection of the  $\text{Pd}^{2+}$  solution or colloidal Pd-NPs and for the colloidal suspension of SNPs,<sup>60</sup> respectively. Both liquid feeds were mixed through a T-static mixer upstream the reactor, leading to a stable Taylor flow. To avoid SNPs precipitation and clogging, a battery-powered portable stirrer was used, ensuring continuous mixing. In the case of the sol-immobilization approach, a pre-formed mixture of Pd-NPs and SNPs was prepared and then pumped into the flow-reactor without irradiation. For the *in situ* photochemical reduction approach, a solution containing  $\text{Pd}^{2+}$ , together with oxalate and citrate salts in a 9 : 1 ratio<sup>36</sup> was mixed with SNPs and pumped through the LED flow reactor. The mixture of photoreductant agents allowed the rapid photochemical reduction of  $\text{Pd}^{2+}$  while ensuring direct contact with the support material.

Using CMC as a stabilizer resulted in a highly viscous and heterogeneous precursor mixture at room temperature, which hindered its flow through the tubular reactor. To overcome this limitation, both sol-immobilization and *in situ* reduction strategies were explored in the tubular flow reactor using PVP as the stabilizer agent to obtain the supported nanocatalyst. Remarkably, Pd-PVP NPs with controlled morphology were successfully formed on the surface of the SNPs within a residence time of only 30 min (Fig. 4b and c).

The sol-immobilization strategy led to the deposition of Pd-PVP NPs with an average size of  $(2.9 \pm 0.7)$  nm and a Pd loading of 3.1 wt% on the SNPs (Pd-PVP-im-F/SNPs, Fig. 4b). Similar to the batch impregnation method (Table SI 4, entry 3), the size of the Pd-NPs remained unchanged throughout the process.

a- Experimental setup of continuous-flow approach

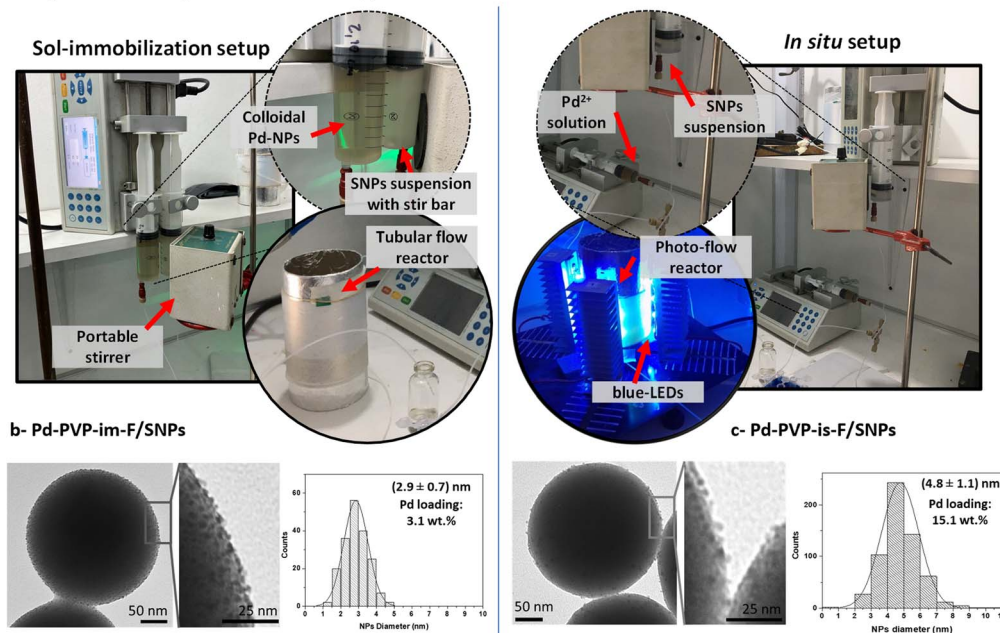


Fig. 4 (a) Experimental setup of continuous flow device used to obtain supported Pd nanocatalysts. TEM images zoom-in and histograms of the supported catalysts obtained through (b) sol-immobilization Pd-PVP-im-F/SNPs and (c) *in situ* reduction Pd-PVP-is-F/SNPs in flow.

Moreover, the Pd loading showed no significant variation compared to the batch approach (Table SI 4, entry 3).

On the other hand, the *in situ* reduction of Pd<sup>2+</sup> salt on SNPs under flow conditions required a higher Pd<sup>2+</sup>/SNPs mass ratio to yield uniform Pd-PVP NPs with a size of (4.8 ± 1.1) nm and a Pd loading of 15.1 wt% (Pd-PVP-is-F/SNPs, Fig. 4c). While the NPs size was comparable to that obtained *via* the *in situ* strategy under batch (Pd-PVP-is-2/SNPs, Table 2, entry 4), the metal loading was lower when the tubular flow reactor was used.

These results demonstrate that the continuous flow approach effectively produces heterogeneous nanocatalysts with a uniform distribution of Pd-NPs and controlled particle sizes on SNPs surfaces, making it a viable alternative to batch synthesis.

### 3.6. Catalytic activity of supported Pd nanocatalysts

The catalytic activity of the supported Pd nanocatalysts was evaluated in the same Suzuki–Miyaura model reaction as for the colloidal Pd-NPs. The results, summarized in Table 3, demonstrate that all materials exhibited excellent catalytic performance towards the formation of the biaryl product **3a**, achieving high yields under mild reaction conditions. However, for the heterogeneous nanocatalysts, the reaction temperature had to be increased to 60 °C and the reaction time extended to 2 h to achieve complete conversion of substrate **1a**.

Each catalytic reaction was carried out using 1 mg of catalyst, corresponding to approximately 0.1–2.0 mol% of Pd. Under these conditions, most of the catalysts achieved yields of **3a** up to 99% (Table 3). Nanocatalysts synthesized *via* the *in situ* photoreduction strategy exhibited higher TOF values (Table 3, entries 2 and 4) than those obtained through sol-immobilization (Table 3, entries 1 and 3). The *in situ* catalyst stabilized with CMC (Pd-CMC-is-1/SNPs) reached the highest TOF value of 356.3 h<sup>−1</sup> (Table 3, entry 2), followed by Pd-PVP-is-1/SNPs with 214.0 h<sup>−1</sup> (Table 3, entry 4). These values are comparable to those reported for other supported nanocatalysts stabilized with carbohydrates polymers.<sup>61</sup> After removal of Pd-CMC-is-1/SNPs catalyst by centrifugation, extraction with ethyl

acetate, and column chromatography, the product **3a** was isolated in 94% of yield.

XPS analysis revealed that the differences in the chemical environments in the two nanocatalysts likely arise from the interaction between Pd species and the functional groups of the polymers, such as carboxyl and hydroxyl groups of CMC and the amide groups in PVP. These interactions can affect critical aspects of the catalytic process, including the adsorption of reactants, the accessibility of catalytic sites (either by partially blocking them or by altering their local environment), and the electronic properties of Pd species on the surface. Consequently, these factors impact on the overall catalytic performance. Therefore, understanding and controlling these polymer–NPs interactions is essential, as they can modulate both catalytic activity and stability.

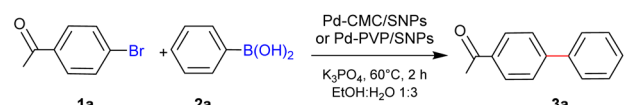
Interestingly, the sol-immobilized catalyst prepared under flow conditions (Pd-PVP-im-F/SNPs, Table 3, entry 5), exhibited an improved performance compared to the batch-synthesized catalyst (Pd-PVP-im/SNPs, Table 3, entry 3). In contrast, the *in situ* flow-photoreduced catalysts (Pd-PVP-is-F/SNPs) showed a lower TOF value than the obtained under batch conditions (Table 3, entry 4 *vs.* entry 6). However, this decrease in TOF is attributed to the higher Pd loading achieved under flow conditions, as complete conversion of **1a** was observed.

Considering these results, the scope of the Suzuki–Miyaura cross-coupling reaction was evaluated with the heterogeneous Pd-CMC-is-1/SNPs nanocatalyst. For that, a series of aryl bromides and aryl iodides (**1b–f**), together with aryl boronic acid (**2a–b**) were evaluated, obtaining biaryls **3a–e** in very good to excellent yields (Table SI 5).

### 3.7. Recyclability tests of supported catalysts

As both catalysts prepared by the *in situ* photoreduction of Pd<sup>2+</sup> using the batch protocol (Pd-PVP-is-1/SNPs and Pd-CMC-is-1/SNPs) were the most active nanocatalysts in the Suzuki–Miyaura cross-coupling reaction for the synthesis biaryl **3a**, their recyclability was evaluated under the previously described conditions. For the recycling experiment, the catalysts were

Table 3 Catalytic activity of supported nanocatalysts in the Suzuki–Miyaura cross-coupling reaction<sup>a</sup>

					
Entry	Catalyst	Catalyst mass (mg)	Pd <sup>b</sup> (mol%)	Yield <sup>c</sup> of <b>3a</b> (%)	TOF <sup>d</sup> (h <sup>−1</sup> )
1	Pd-CMC-im-1/SNPs	1.10	0.09	22	164.8
2	Pd-CMC-is-1/SNPs	1.12	0.14	99	356.3
3	Pd-PVP-im/SNPs	1.11	0.28	52	98.7
4	Pd-PVP-is-1/SNPs	1.06	0.23	95	214.0
5	Pd-PVP-im-F/SNPs	1.19	0.29	93	169.6
6	Pd-PVP-is-F/SNPs	1.68	2.0	94	24.8

<sup>a</sup> Reaction conditions: 0.12 mmol **1a**, 0.18 mmol **2a**, 0.37 mmol K<sub>3</sub>PO<sub>4</sub>, 1.0 mg of supported nanocatalyst, ethanol:water 1 : 3. <sup>b</sup> Referred to initial moles of **1a**. <sup>c</sup> Quantified by GC analysis with benzophenone as internal standard. <sup>d</sup> TOF = mole of substrate **1a** converted/(mole of Pd\**h*).



recovered by centrifugation after 2 h of reaction, washed twice with water, and reused in subsequent runs without further purification or activation. The results presented in Fig. 5 indicate that in both cases high yields of product **3a** were consistently obtained over successive cycles under mild conditions. These nanomaterials therefore demonstrated excellent catalytic activity and recyclability for at least 3 consecutive cycles. However, following the fourth cycle, a progressively decrease in activity was observed for Pd-CMC-is-1/SNPs (Fig. 5).

In addition, Pd leaching was assessed by ICP-MS analysis of the aqueous reaction media. Notably, only a low Pd leaching was detected after the first catalytic cycle, with 0.066 ppm of Pd for Pd-PVP-is-1/SNPs and 0.071 ppm of Pd for Pd-CMC-is-1/SNPs. In subsequent cycles, even after the fifth cycle, Pd concentration was below the limit of detection (LOD), confirming the strong immobilization of Pd onto the SNP surface through the *in situ* photoreduction strategy. These values are lower than the residual Pd levels allowed in pharmaceutical products (below 10 ppm).<sup>62,63</sup>

The analysis of the recovered catalysts through TEM micrographs (Fig. SI 15) showed a partial degradation of the silica support and encapsulation of the Pd-NPs in the silica matrix. These findings suggest that the SNP support undergoes some degradation over successive cycles, likely due to interactions with  $K_3PO_4$ . It is well known that certain bases can react with the acidic sites present on silica surfaces, leading to surface degradation.<sup>64</sup>

However, the Pd-NPs are still active and attached on the support after several reaction cycles. Thus, degradation of the SNP support may lead to partial encapsulation of the Pd-NPs by a silica phase, potentially obstructing access to the metallic active sites and reducing their catalytic activity.

These supported Pd-NPs represent a promising and potentially safe option for the synthesis of pharmaceutically relevant molecules. The SNP proved to be a suitable model for exploring alternative strategies to obtain heterogeneous nanocatalysts. Nevertheless, we are currently evaluating alternative supports

capable of resisting the basic reaction conditions, to enhance long-term catalyst stability.

## 4 Conclusions

In this work, a simple and environmentally friendly photochemical method was developed to synthesize small Pd-NPs, both as colloidal and as supported heterogeneous catalysts. The synthesis avoided the use of toxic and hazardous chemicals and solvents, providing a green route for the preparation of Pd nanocatalysts under both batch and continuous flow processes. Colloidal Pd-NPs were effectively stabilized using PVP and biomass-derived CMC. Among the colloidal systems, Pd-CMC NPs achieved the highest TOF in the Suzuki–Miyaura cross-coupling reaction, highlighting the potential of bio-based stabilizers as sustainable alternatives to oil-derived ones.

The photochemical strategy was also successfully extended to produce supported Pd-NPs on functionalized  $SiO_2$ . The *in situ* photoreduction approach proved to be a straightforward and efficient method, particularly effective for producing well-dispersed, small Pd-NPs on the SNPs surface. Furthermore, this approach yielded the most catalytically active materials. Notably, CMC demonstrated outstanding stabilization capacity, enhancing catalytic performance. Recyclability tests confirmed that Pd-NPs maintained high catalytic activity over several reaction cycles without Pd leaching.

Continuous-flow setups were also explored, achieving materials with catalytic performance comparable to batch obtained ones for supported Pd-NPs stabilized with PVP. This photo-induced and eco-friendly methodology, demonstrates the advantages of combining simple protocols with sustainable reagents for synthesis of heterogeneous Pd nanocatalysts. The use of biodegradable, bio-based materials align with green chemistry principles, while the integration of continuous-flow technology enhances reaction control, efficiency, and scalability. Overall, this work provides the groundwork for the sustainable, and large-scale production of catalytic nanomaterials with broad application potential.

## Author contributions

Conceptualization: GOM, PMU and SSC; formal analysis: SMSC, IDC, FP, PMU, GOM, and SEM; funding acquisition: PMU, GOM, SSC and SEM; investigation: IDC, SMSC, FP, PMU, and GOM; methodology: IDC, SMSC, FP, PMU, and GOM; project administration and supervision: PMU, GOM, and SEM; writing – original draft: PMU, SSC and GOM; writing – review & editing: IDC, SMSC, FP, PMU, GOM, and SEM.

## Conflicts of interest

The authors declare no competing financial interest.

## Data availability

The authors have cited additional references within the SI.<sup>22,37,41–44,65–71</sup> SI data to this article with additional experimental

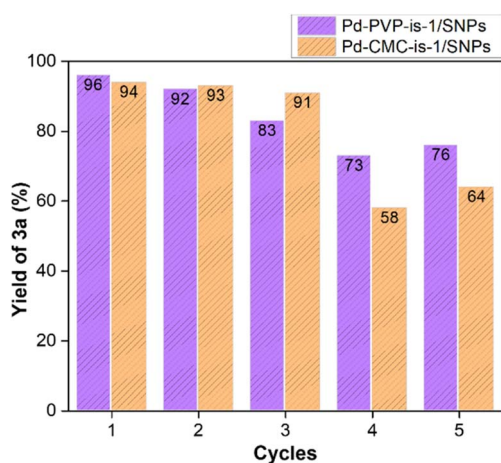


Fig. 5 Recycling tests of supported catalysts prepared by *in situ* photoreduction using PVP (Pd-PVP-is-1/SNPs) and CMC (Pd-CMC-is-1/SNPs) in the Suzuki–Miyaura cross-coupling reaction.



details and characterization data can be found online. Supplementary information is available. See DOI: <https://doi.org/10.1039/d5ra05019g>.

## Acknowledgements

The authors acknowledge research support from CONICET (grant number: CONICET, PIP No. 0100271), FONCYT (grant number FONCYT-program, PICT 2021 – 00651 and PICT 2020 SERIE A – 03636), SECyT (grant number: SECyTUNC, R. SECYT 366/16, N: 05/CP15). Della-Cagnoletta I gratefully acknowledges CONICET for her fellowship. Martín SE, Uberman PM, Soria-Castro SM, Politano F., and Oksdath-Mansilla G. are researchers from CONICET. The authors would like to acknowledge the assistance from CONICET and Universidad Nacional de Córdoba (UNC), both of which provided facilities for this research. The authors are grateful to Prof. Veronica Brunetti (INFIQC) for their valuable assistance with XPS measurements.

## Notes and references

- 1 A. Biffis, P. Centomo, A. Del Zotto and M. Zecca, *Chem. Rev.*, 2018, **118**, 2249–2295.
- 2 M. A. Ahmad, M. Adeel, N. Shakoor, R. Javed, M. Ishfaq, Y. Peng, M. Zain, I. Azeem, I. Ali, M. Usman, Z. Wu, G. Gohari, M. Xu, Y. Rui, Z. Zhang, J. C. White and X. Deng, *Sci. Total Environ.*, 2023, **894**, 164861.
- 3 A. Chatterjee and T. R. Ward, *Catal. Lett.*, 2016, **146**, 820–840.
- 4 N. Baig, I. Kammakakam, W. Falath and I. Kammakakam, *Mater. Adv.*, 2021, **2**, 1821–1871.
- 5 V. P. Aswathi, S. Meera, C. G. A. Maria and M. Nidhin, *Nanotechnol. Environ. Eng.*, 2023, **8**, 377–397.
- 6 A. García-Quintero and M. Palencia, *Sci. Total Environ.*, 2021, **793**, 148524.
- 7 P. K. Dikshit, J. Kumar, A. K. Das, S. Sadhu, S. Sharma, S. Singh, P. K. Gupta and B. S. Kim, *Catalysts*, 2021, **11**, 1–35.
- 8 A. Leal-Duaso, I. Favier, D. Pla, E. Pires and M. Gómez, *ACS Sustain. Chem. Eng.*, 2021, **9**, 6875–6885.
- 9 M. N. Nadagouda and R. S. Varma, *Green Chem.*, 2008, **10**, 859–886.
- 10 M. S. Bakshi, *Cryst. Growth Des.*, 2016, **16**, 1104–1133.
- 11 G. Albano, A. Petri and L. A. Aronica, *Catalysts*, 2023, **13**, 210.
- 12 A. Khazaei, S. Rahmati, Z. Hekmatian and S. Saeednia, *J. Mol. Catal. A: Chem.*, 2013, **372**, 160–166.
- 13 T. Baran, *Carbohydr. Polym.*, 2018, **195**, 45–52.
- 14 N. Yilmaz Baran, T. Baran and A. Menteş, *Carbohydr. Polym.*, 2018, **181**, 596–604.
- 15 Z. Dolatkah, S. Javanshir and A. Bazgir, *J. Iran. Chem. Soc.*, 2019, **16**, 1473–1481.
- 16 S. Kamel and T. A. Khatatb, *Cellulose*, 2021, **28**, 4545–4574.
- 17 Z. Wang, S. Lü, F. Yang, S. M. F. Kabir, S. Mahmud and H. Liu, *Colloids Surf., A*, 2021, **628**, 127345.
- 18 M. Niakan, M. Masteri-Farahani, H. Shekaari and S. Karimi, *Carbohydr. Polym.*, 2021, **251**, 117109.
- 19 A. K. Zharmagambetova, E. T. Talgatov, A. S. Auyezkhanova, F. U. Bukharbayeva and A. I. Jumekeyeva, *Catalysts*, 2023, **13**, 1403.
- 20 Y. Dong, X. Wu, X. Chen and Y. Wei, *Carbohydr. Polym.*, 2017, **160**, 106–114.
- 21 A. A. Mekkaoui, H. Orfi, K. Bejtka, M. Laayati, S. A. Labyad, L. El Firdoussi, C. F. Pirri, A. Chiodoni and S. El Houssame, *Environ. Sci. Pollut. Res.*, 2023, **30**, 81619–81634.
- 22 J. Xiao, Z. Lu and Y. Li, *Ind. Eng. Chem. Res.*, 2015, **54**, 790–797.
- 23 J. Liu, F. He, E. Durham, D. Zhao and C. B. Roberts, *Langmuir*, 2008, **24**, 328–336.
- 24 J. Zhou, Y. Wu, Y. Liu, N. Li, Z. Yang, J. Ying, X. Ren, T. Zhang, W. Xu, J. Chen, X. Cao, R. Yu and M. Zeng, *ChemCatChem*, 2025, **17**, e202401358.
- 25 S. Zhang, Y. Huang, T. Lin, M. Xue, S. Liu, H. Deng and Y. Li, *Cellulose*, 2025, **32**, 1645–1665.
- 26 V.-D. Le, T. K. C. Huynh, V. N. Dao, C.-H. Dang and T. Y. N. Le, *RSC Adv.*, 2025, **15**, 10534–10546.
- 27 T. A. Thiel, R. Y. Parapat, M. Schroeter and M. Schwarze, *Chem.-Eur. J.*, 2025, **31**(2), e202402952.
- 28 P. Gómez-López, A. Puente-Santiago, A. Castro-Beltrán, L. A. Santos do Nascimento, A. M. Balu, R. Luque and C. G. Alvarado-Beltrán, *Curr. Opin. Green Sustain. Chem.*, 2020, **24**, 48–55.
- 29 N. Joudeh, A. Saragliadis, G. Koster, P. Mikheenko and D. Linke, *Front. Nanotechnol.*, 2022, **4**, 1–24.
- 30 F. N. Figueroa, J. Torres, L. Campagno, M. Calderón, F. L. Alovero, M. Strumia, M. C. García and G. Oksdath-Mansilla, *ACS Appl. Eng. Mater.*, 2024, **2**, 2397–2413.
- 31 A. A. Alshehri and M. A. Malik, *Biomolecules*, 2020, **10**, 1–24.
- 32 J. S. Santana and S. E. Skrabalak, *Adv. Energy Mater.*, 2020, **10**, 1–14.
- 33 E. J. Roberts, L. R. Karadaghi, L. Wang, N. Malmstadt and R. L. Brutchey, *ACS Appl. Mater. Interfaces*, 2019, **11**, 27479–27502.
- 34 B. Gutmann, D. Cantillo and C. O. Kappe, *Angew. Chem., Int. Ed.*, 2015, **54**, 6688–6728.
- 35 F. Mäsing, H. Nüsse, J. Klingauf and A. Studer, *Org. Lett.*, 2018, **20**, 752–755.
- 36 E. D. Díaz-Vázquez, S. M. Soria-Castro, I. Della-Cagnoletta, S. E. Martín, G. Oksdath-Mansilla and P. M. Uberman, *React. Chem. Eng.*, 2022, **7**, 957–967.
- 37 J. V. Kingston and J. G. Verkade, *J. Org. Chem.*, 2007, **72**, 2816–2822.
- 38 G. Li, L. Liu, Y. Sun and H. Liu, *J. Clust. Sci.*, 2018, **29**, 1193–1199.
- 39 K. Park, S. S. Park, Y. H. Yun and C. S. Ha, *J. Porous Mater.*, 2017, **24**, 1215–1225.
- 40 J. Xiao, Z. Lu, Z. Li and Y. Li, *Appl. Organomet. Chem.*, 2015, **29**, 646–652.
- 41 Y. Li, L. Xu, B. Xu, Z. Mao, H. Xu, Y. Zhong, L. Zhang, B. Wang and X. Sui, *ACS Appl. Mater. Interfaces*, 2017, **9**, 17155–17162.
- 42 T. N. Ansari, S. Sharma, S. Hazra, J. B. Jasinski, A. J. Wilson, F. Hicks, D. K. Leahy and S. Handa, *JACS Au*, 2021, **1**, 1506–1513.



- 43 T. Maegawa, Y. Kitamura, S. Sako, T. Udzu, A. Sakurai, A. Tanaka, Y. Kobayashi, K. Endo, U. Bora, T. Kurita, A. Kozaki, Y. Monguchi and H. Sajiki, *Chem.–Eur. J.*, 2007, **13**, 5937–5943.
- 44 D. Yu, B. Jie, J. Wang and C. Li, *J. Catal.*, 2018, **365**, 195–203.
- 45 D. Li, F. Miao, J. Chen, Z. Liu, Z. Wang and Y. Wang, *Processes*, 2025, **13**, 339.
- 46 P. M. Uberman, L. A. Pérez, S. E. Martín and G. I. Lacconi, *RSC Adv.*, 2014, **4**, 12330–12341.
- 47 M. Gholinejad, Z. Naghshbandi and C. Nájera, *ChemCatChem*, 2019, **11**, 1792–1823.
- 48 P. Veerakumar, P. Thanasekaran, K. L. Lu, S. Bin Liu and S. Rajagopal, *ACS Sustain. Chem. Eng.*, 2017, **5**, 6357–6376.
- 49 M. Aksoy, H. Kilic, B. Nisanci and Ö. Metin, *Inorg. Chem. Front.*, 2021, **8**, 499–545.
- 50 D. Zhang, H. Cai, Y. Su, W. Sun, D. Yang and G. A. Ozin, *Chem Catal.*, 2022, **2**, 1893–1918.
- 51 J. Pritchard, M. Piccinini, R. Tiruvalam, Q. He, N. Dimitratos, J. A. Lopez-Sanchez, D. J. Morgan, A. F. Carley, J. K. Edwards, C. J. Kiely and G. J. Hutchings, *Catal. Sci. Technol.*, 2013, **3**, 308–317.
- 52 M. M. Elsutohy, A. Selo, V. M. Chauhan, S. J. B. Tendler and J. W. Aylott, *RSC Adv.*, 2018, **8**, 35840–35848.
- 53 R. I. Teixeira, N. C. De Lucas, S. J. Garden, A. E. Lanterna and J. C. Scaiano, *Catal. Sci. Technol.*, 2020, **10**, 1273–1280.
- 54 N. Hassan, V. Cabuil and A. Abou-Hassan, *Angew. Chem., Int. Ed.*, 2013, **52**, 1994–1997.
- 55 L. Prati and A. Villa, *Catalysts*, 2011, **2**, 24–37.
- 56 M. Guadalupe Martin, J. M. Lázaro-Martínez, S. E. Martín, P. M. Uberman and M. E. Budén, *Chem.–Eur. J.*, 2024, **30**, e202303382.
- 57 M. Madani, S. Hosny, D. M. Alshangiti, N. Nady, S. A. Alkhursani, H. Alkhaldi, S. A. Al-Gahtany, M. M. Ghobashy and G. A. Gaber, *Nanotechnol. Rev.*, 2022, **11**, 731–759.
- 58 J. García-Aguilar, M. Navlani-García, Á. Berenguer-Murcia, K. Mori, Y. Kuwahara, H. Yamashita and D. Cazorla-Amorós, *Langmuir*, 2016, **32**, 12110–12118.
- 59 N. Sakurada, K. Kobayashi, Y. Abe, K. Niwa, T. Yokoyama, T. Yamada, T. Ikawa and H. Sajiki, *ChemSusChem*, 2025, **18**, e202401859.
- 60 C. Mendoza, N. Emmanuel, C. A. Páez, L. Dreesen, J. C. M. Monbaliu and B. Heinrichs, *ChemPhotoChem*, 2018, **2**, 890–897.
- 61 H. Ahmad, *J. Clust. Sci.*, 2022, **33**, 421–438.
- 62 International Council for Harmonisation of Technical Requirements for Pharmaceuticals for Human Use (ICH), *ICH Harmonised Tripartite Guideline Q3D(R1): Guideline for Elemental Impurities*, ICH, 2020.
- 63 C. S. Horbaczewskyj and I. J. S. Fairlamb, *Org. Process Res. Dev.*, 2022, **26**, 2240–2269.
- 64 Y. L. Shi and T. Asefa, *Langmuir*, 2007, **23**, 9455–9462.
- 65 K. Park, S. S. Park, Y. H. Yun and C. S. Ha, *J. Porous Mater.*, 2017, **24**, 1215–1225.
- 66 A. Fihri, D. Luat, C. Len, A. Solhy, C. Chevrin and V. Polshettiwar, *Dalton Trans.*, 2011, **40**, 3116–3121.
- 67 Q. Li, L. Zhang, J. Bao, H. Li, J. Xie and J. Lang, *Appl. Organomet. Chem.*, 2014, **28**, 861–867.
- 68 N. Liu, C. Liu and Z. Jin, *Green Chem.*, 2012, **14**, 592–597.
- 69 X. Li, Y. Liu, L. Zhang, Y. Dong, Q. Liu, D. Zhang, L. Chen, Z. Zhao and H. Liu, *Green Chem.*, 2022, **24**, 6026–6035.
- 70 S. Bhadra, W. I. Dzik and L. J. Goossen, *J. Am. Chem. Soc.*, 2012, **134**, 9938–9941.
- 71 M. E. John, M. J. Nutt, J. E. Offer, J. A. Duczynski, K. Yamazaki, T. Miura, S. A. Moggach, G. A. Koutsantonis, R. Dorta and S. G. Stewart, *Angew. Chem., Int. Ed.*, 2025, **64**, e202504108.

